Superior Energy Dissipation by Ultra-thin Semi-

crystalline Polymer Films Under Supersonic

Micro-Projectile Impacts

Jizhe Cai, and Ramathasan Thevamaran*

Department of Engineering Physics

University of Wisconsin-Madison

1500 Engineering Dr, Madison, WI 53706, USA

E-mail: thevamaran@wisc.edu

ABSTRACT: Distinct deformation mechanisms that emerge in nanoscale enable the

nanostructured materials to exhibit outstanding specific mechanical properties. Here, we

present superior microstructure- and strain-rate-dependent specific penetration energy (up to

~3.8 MJ kg⁻¹) in semi-crystalline poly(vinylidene fluoride-co-trifluoroethylene) (P(VDF-

TrFE)) thin-films subjected to high-velocity (100 m s⁻¹ to 1 km s⁻¹) micro-projectile (diameter:

9.2 µm) impacts. The geometric-confinement-induced nanostructural evolutions enable the

sub-hundred-nanometers-thick P(VDF-TrFE) films to achieve high specific penetration energy

with high strain delocalization across broad impact velocity range—superior to both bulk

protective materials and previously-reported nanomaterials. This high specific penetration

energy arises from the substantial stretching of the two-dimensionally-oriented highly-mobile

polymer chains which engage abundant viscoelastic and viscoplastic deformation mechanisms

1

that are further enhanced by the intermolecular dipole-dipole interactions. These key findings provide insights for using nanostructured semi-crystalline polymers in the development of lightweight high-performance soft armors for extreme engineering applications.

KEYWORDS: energy dissipation, geometric confinement, semi-crystalline polymer, supersonic impact, soft armor

Making strong, tough, light-weight and soft protective materials, typically called "armor", has always been a major pursuit throughout history for human survival in everincreasing external dangers and threats. 1 With the emergence of nanotechnology, discovery of new nanomaterials has offered greater number of opportunities to develop high-performance armor with outstanding "specific" mechanical properties²⁻⁶ and novel failure-proof toughening mechanisms.⁷⁻¹² High specific energy dissipation and rapid strain delocalization are critical for mitigating high-speed projectile impacts.^{8, 9, 13} The specific energy dissipation is the kinetic energy of a projectile dissipated by a unit weight of material upon impact and the strain delocalization characterizes how far the impact-induced displacement field propagates in the material. Benefiting from the development of laser-induced micro-projectile impact testing (LIPIT) and nanoscale characterization approaches, the distinct protective mechanisms of various nanomaterials have recently been studied. 8, 9, 13-15 The multi-layer graphene (MLG) has initially been shown to exhibit higher specific penetration energy compared to macroscopic protective materials, due to its superior in-plane sound speed, strength, and stiffness. 8 Following this direction, graphene-oxide/silk fibroin nanocomposite thin-films and carbon nanotube yarns have been developed, which also showed improvement in specific penetration energy from the high-performance nanoscale constituents and their interfacial interactions. 13, 15 Compared to employing these stiff nanomaterials, surprisingly, ultra-thin polymer films exhibit even higher specific penetration energy due to the size-dependent energy dissipation mechanisms, 9, 14, however, this behavior is highly dependent on high-speed projectile impact induced heating.

Semi-crystalline polymers, such as, polyethylene (PE), poly(p-phenylene terephthalamide) (PPTA) and polytetrafluoroehylene (PTFE) that are widely used in highstrain-rate protective applications, exhibit more complex rate- and temperature-dependent deformation mechanisms that stem from their microstructure, including crystallinity and molecular conformation. 16-18 The semi-crystalline polymers are usually treated as two-phase structure with "rigid" crystalline phase distributed within "soft" amorphous matrix. The thin (100 nm - 1000 nm) and ultra-thin (less than 100 nm) semi-crystalline polymer films have attracted recent attention due to their unique geometric-confinement-induced microstructural evolutions and physical property changes. 19-21 Similarly, experimental investigations on nanofibers made of poly(vinylidene fluoride-co-trifluoroethylene) (P(VDF-TrFE))—a widely used piezoelectric polymer—showed that the geometric confinement of fiber diameter to subhundred nanometers leads to outstanding Young's modulus (~80 GPa) ²², and when the nanofibers are twisted into yarns, the yarns exhibit high toughness (~98 J/g) ²³ due to the piezoelectrically enhanced interactions among fibers. However, the effects of geometricconfinement induced microstructural evolutions and their intrinsic effects on the dynamic behavior of semi-crystalline polymers remains elusive because of the limitations in small scale dynamic testing techniques. Successful development of soft protective materials using such polymers require a fundamental understanding of their underlying structure-property relations in dynamic regime.

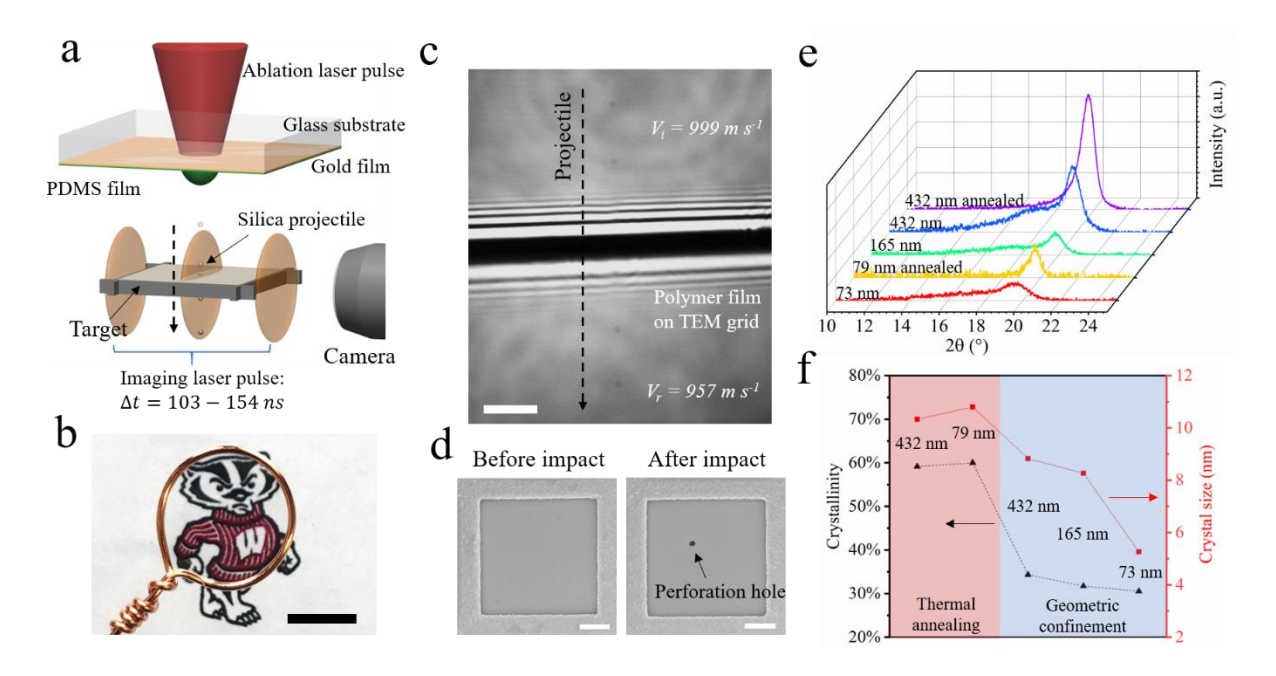


Figure 1. (a) Illustration of the LIPIT. (b) A 73nm-thick transparent P(VDF-TrFE) film mounted on copper hoop. Scale bar = 1 cm. (c) Perforation process of a 73nm-thick film by a microprojectile. Scale bar = $100 \ \mu m$. (d) SEM images of the polymer film before and after projectile perforation. Scale bar = $50 \ \mu m$. (e) X-ray diffraction spectra of P(VDF-TrFE) films of different thicknesses with and without thermal annealing, and (f) Calculated crystallinity and crystal size of P(VDF-TrFE) with different fabrication conditions.

Here, we use P(VDF-TrFE) as a model material system to study the relationship between the nanostructure and dynamic properties of semi-crystalline polymers under ultrahigh-strain-rate deformations (up to 10⁸ s⁻¹), by an advanced LIPIT system built at the University of Wisconsin-Madison (Figure 1a). Free-standing P(VDF-TrFE) films fabricated by spin-coating (Figure 1b) in different thicknesses, from 73 nm to 432 nm, were deposited on 100-square-mesh Ni TEM grids and placed ~500 μm away from the projectile launch pad—a glass substrate coated first with a 50 nm gold layer (laser ablation layer) followed by a 25 μm-thick cross-linked polydimethylsiloxane (PDMS) layer. Individual silica projectiles (diameter ~9.2 μm) deposited on the launch pad were selectively launched by the rapid expansion of PDMS film via laser-ablation-induced gold vaporization (Figure 1c).⁸ A broad range of projectile impact velocities from 100 m s⁻¹ to 1 km s⁻¹ was achieved by varying the ablation laser energy. The impact of supersonic (up to Mach 3) micro-projectile on the nanoscale polymer films results in high-strain-rate (~10⁷ – 10⁸ S⁻¹; see supporting information)

deformation of the films ^{9, 13}. The film morphology before and after perforation (Figure 1d) were imaged in high resolution scanning electron microscopy (SEM) to investigate the deformation mechanisms. The impact/perforation process of the films was recorded in an ultra-fast multi-exposure image by a microscope camera illuminated by pico-second white-laser pulses at an interval of 103-154 ns. The projectile speeds before and after perforation of the target were calculated from the measured distance between adjacent snapshots of projectiles divided by the time interval between consecutive imaging laser pulses and corrected for deceleration due to air-drag (drag coefficient measurement and projectile speed correction methods are provided in the supporting information and follows the supporting information of Ref [9]).

We control the microstructure of P(VDF-TrFE) films through size (thickness) confinement and thermal annealing, which modifies the crystalline structure and polymer chain conformation within the semi-crystalline polymer films. $^{19, 24}$ The XRD peak that appears at $20\sim19.8^{\circ}$ originates from the (110)/(200) reflection planes of β -phase crystallites in the film (Figure 1e and 1f)). When the film thickness is decreased from 432 nm to 73 nm, a reduction in both crystallinity and crystal size within the film is evident, indicating the geometric-confinement-induced aversion to crystallization during fabrication, which has also been observed previously in spin-coated semi-crystalline polymer films, $^{19, 25-27}$ and was attributed to the strain incompatibility between adjacent crystalline domains that favors amorphous structure. Moreover, the polymer chain backbone and crystal lamellae tend to orient in plane as the polymer film thickness is decreased to sub-100 nm scale. Me post-fabrication thermal annealing increases the crystallinity and crystal size of both thick (432 nm) and ultrathin (79 nm) P(VDF-TrFE) films to a comparable level (Figure 1f) (see calculations in supporting information).

The post-impact SEM images of damage zone of the polymer films with different crystallinities and impact speeds are shown in Figure 2a. The annealed thick polymer films

show the formation of radial mature fibrillated micro-crazes around the perforation area with stretched and broken fibrils connecting the two edges of the crazes (see inset of Figure 2a(iii)), indicating a brittle failure process under high-speed (200 m s⁻¹ to 1 km s⁻¹) projectile impacts. The radial micro-craze growth from the perforation hole with still load-bearing stretched nanofibrils demonstrates the roles played by the strong tangential tensile forces during the equibiaxial stretching of the thin film. In medium- to high-speed impacts (600 m s⁻¹–1 km s⁻¹), some polymer melt is found around the impact region, which was caused by the impact-induced adiabatic heating of the polymer.⁹

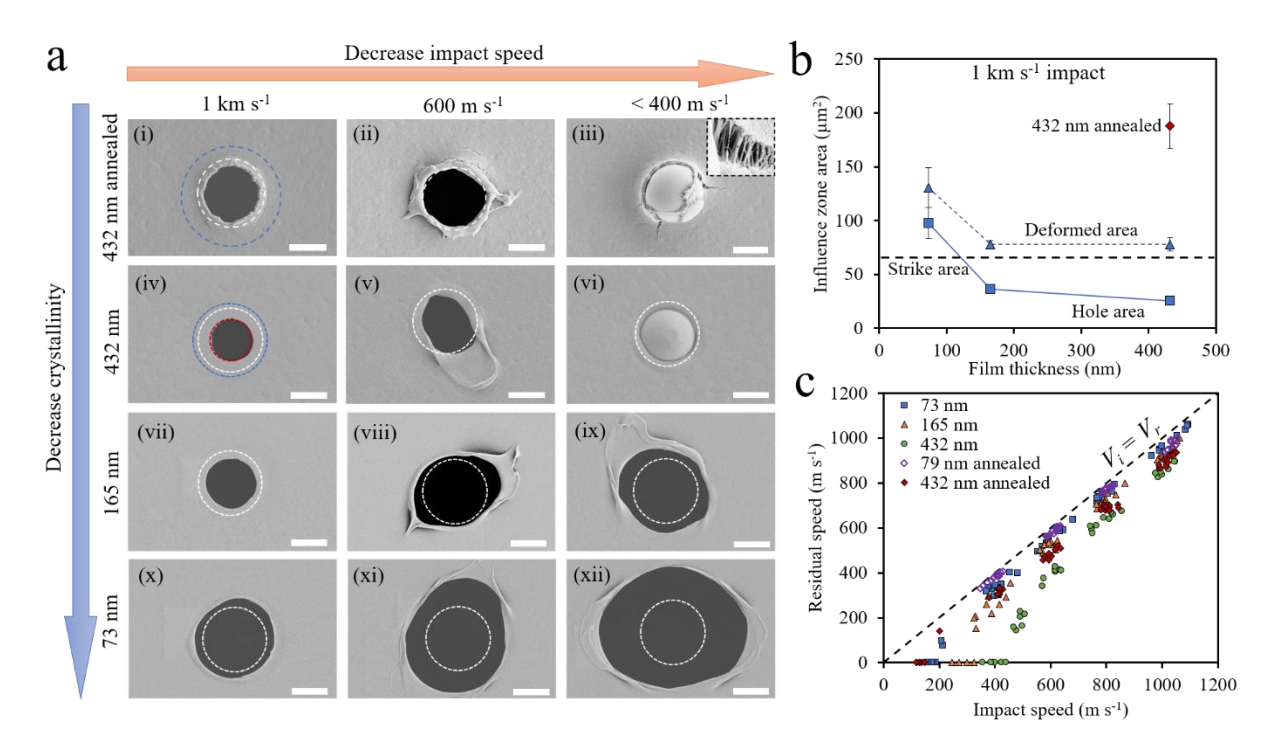


Figure 2. (a) SEM images of perforated films with different crystallinities and impact speeds; the white, blue, and red dashed circles indicate the projectile size, impact influence (deformation) zone, and perforation hole, respectively. For the films that exhibited brittle behavior, the impact influence zone encircles the longest crazes around the perforation hole and the influence zone in the films that deformed in a ductile manner is directly measured from the electron channeling contrast in SEM images. Scale bar = 5 μ m. (b) Influence zone area corresponding to different films from 1 km s⁻¹ impact, and (c) Post-penetration residual speed of the projectile as a function of impact speed for different samples.

The non-annealed P(VDF-TrFE) thin-films with same thickness (432 nm) as the annealed sample exhibit ductile behavior as evident in folded and significantly stretched film flaps around the perforation hole, Figure 2a(v). This brittle-to-ductile transition in failure

mechanism is associated with the decrease in both crystallinity (59% to 34%) and crystal size (10.3 nm to 8.8 nm). Since the segmental mobility of polymer chains in amorphous phase of the semi-crystalline polymers is highly restricted by the nearby crystalline domains, the reduction of such constraints in non-annealed films contribute to the improved polymer chain mobility, hence result in a ductile behavior. It is found that the annealed 432-nm-thick films with brittle failure exhibit twice as large influence zone than the non-annealed pristine 432-nm-thick films (Figure 2b) (influence zone in brittle film is characterized by the farthest propagating craze). Since the T_g of P(VDF-TrFE) is -36 $^{\circ}$ C, 30 the as-fabricated pristine polymer films are in rubbery state at room temperature. During impact by the spherical projectile, a strong equibiaxial tensile stress develops within the impact zone of the film, which stretches the film in a conical shape (Figure 2a(vi)), evidenced by the near circular shape of perforation holes in films with all three thicknesses (Figure 2a(iv, vii, x)). These deformation characteristics are distinct from the damage zone morphology of annealed films with fractured edges and radial crazes, and of the previously studied glassy PS polymer thin-films with numerous radial and tangential crazes.

As the film thickness decreases to 73nm, an increase in the perforation hole area and the impact influence zone are evident (Figure 2b and S2), suggesting film-thickness-dependent dynamic deformation response of the polymer films. This enlarged deformed area implies higher strain delocalization that occurred in the thinner films during projectile penetration. The deformation and failure mechanism of 73 nm-thick films change as the projectile impact speed is decreased from 1 km s⁻¹ to <400 m s⁻¹, with strain rate decreases from 1×10⁸ s⁻¹ to 2×10⁷ s⁻¹, as seen in the circular to oval shape change of the perforation hole, increase in the perforation hole area, and the extent of stretched film flaps (Figure 2a(x-xii)), which also indicate the significant contribution of viscoelastic and viscoplastic deformations. The Figure 2c shows the post-penetration residual speed of the projectile corresponding to each impact speed. The

critical impact speed necessary to perforate the films with 73, 165, and 423 nm thickness are \sim 186, 325, and 440 m s⁻¹, respectively. The annealed 432 nm and 79 nm films are penetrated at much lower critical speeds (<200 m s⁻¹) compared to the pristine films with same thickness.

The penetration energy (E_p) of the material during projectile perforation is calculated from the kinetic energy loss of the projectile (ΔKE) : $E_p = \Delta KE = \frac{1}{2} m_p (v_i^2 - v_r^2)$, where m_p is the mass of the projectile, and v_i and v_r are the impact and residual speeds of projectile right before and after perforation⁸ (calculated accounting for the air-drag-induced projectile deceleration, see supporting information). To quantitatively compare different materials tested at different sample thicknesses and with various projectile sizes, the specific penetration energy (E_p^*) is calculated by normalizing the penetration energy by the mass of the polymer films within the projectile strike area (m_{plug}) , $E_p^* = E_p/(\rho A_s t)$, with polymer density ρ , strike area A_s (projected area of the projectile on the film), and sample thickness t. 9,13

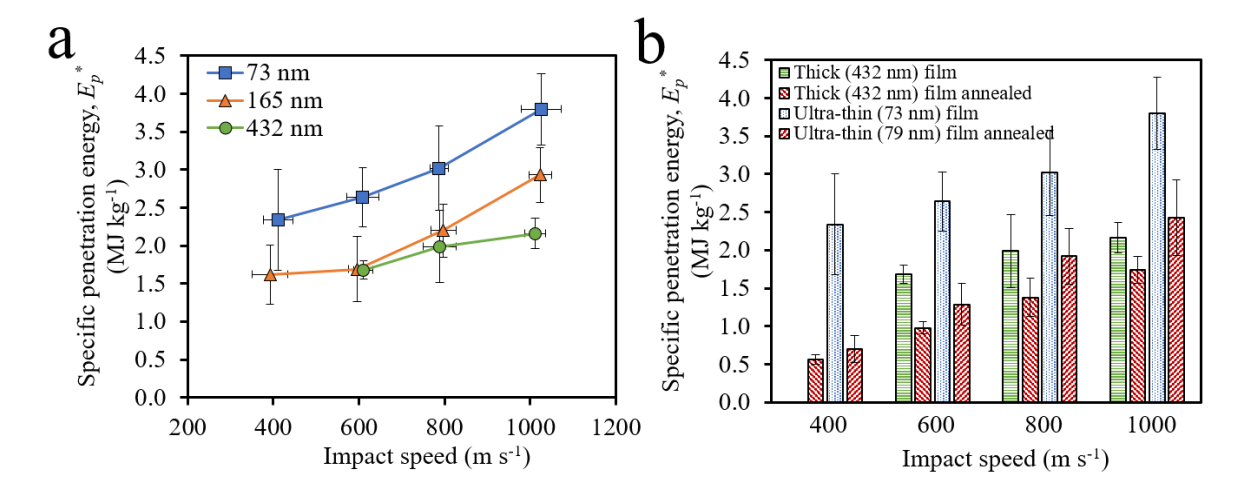


Figure 3. (a) The specific penetration energy (E_p^*) of P(VDF-TrFE) films with different thicknesses, and (b) the E_p^* of as-fabricated and thermal-annealed P(VDF-TrFE) films impacted at different speeds.

The Figure 3a shows the E_p^* of the P(VDF-TrFE) films as a function of projectile impact speed. The substantial film stretching in pristine films dissipates large amount of kinetic energy via highly nonlinear viscoelastic deformation, yielding, and viscoplastic flow at large strains

and high strain rates, similar to other bulk semi-crystalline polymers such as PTFE.¹⁷ The impact-induced adiabatic heating of polymer samples within the strike area rapidly raises its local temperature and causes a viscoelastic melt flow within the strike region. Compared to glassy PS that exhibited much of the energy dissipation through such melt flow,9 the pristine rubbery P(VDF-TrFE) films dissipate significantly more energy through film's homogeneous viscoelastic and viscoplastic deformations that occur far beyond the strike region even at low impact velocities. As the impact velocity is increased, the E_p^* increases, potentially from the rate-dependent yield and hardening behavior in polymers. 31, 32 When the film thickness is reduced to sub-100 nm, significant microstructure- and strain-rate-dependent dynamic response emerges. The 73-nm-thick P(VDF-TrFE) films impacted at 1 km s⁻¹ exhibit the highest E_p^* of 3.80 ± 0.47 MJ kg⁻¹ (Figure 3a), which is $\sim 76\%$ higher than that of the 432-nm-thick films. The annealed samples exhibit much lower E_p^* in the entire range of projectile impact speeds (Figure 3b). Considering its larger influence zone (Figure 2b), the brittle failure with highly localized craze growth is ineffective in dissipating kinetic energy compared to pristine films that exhibit ductile deformation. The ultra-thin (79 nm) annealed film, exhibits slightly higher E_p^* than the thick (432 nm) annealed films and the difference in their E_p^* increases as the projectile impact speed is increased.

The geometric confinement of P(VDF-TrFE) in ultra-thin films induces considerable microstructural evolutions as illustrated in Figure 4a. The bulk polymer or thick films have greater number of large-sized crystalline domains (higher crystallinity) randomly distributed within the amorphus polymer matrix, which constrains polymer chain mobility, especially within the interior regions. Higher crystallinity increases the modulus and decreases the ductility of bulk semi-crystalline polymers.²⁴ The mobility of less-mobile polymer chains in thick films are further reduced at higher strain rates because of chain stiffening,³³ which results in rather brittle-like localized deformation. In contrast, the thickness of the ultra-thin (73 nm)

films are comparable to the end-to-end distance (46 nm) of the polymer chains in amorphous regions, which amplifies the microstructural evolution. This geometric confinement results in reduction of crystallinity and crystalline domain sizes and increases the fraction of polymer chains in amorphous phase within the interior of the sample. Additionally, the fraction of lessentangled highly-mobile polymer chains in near-free-surface region significantly increases with their preferential orientation parallel to the film surface, 28,29,34 which results in higher strainto-failure of the film. The effects of mobile near-surface chains in ultra-thin films is also evident in the annealed films, where the ultra-thin annealed films exhibit higher E_p compared to the annealed thick films, regardless of their similar crystallinity (Figure 1f). When the projectile impact velocity is increased, the contribution of near-surface chains are further enhanced by the impact-induced adiabatic heating and the resultant energy dissipation from viscoelastic melt flow.

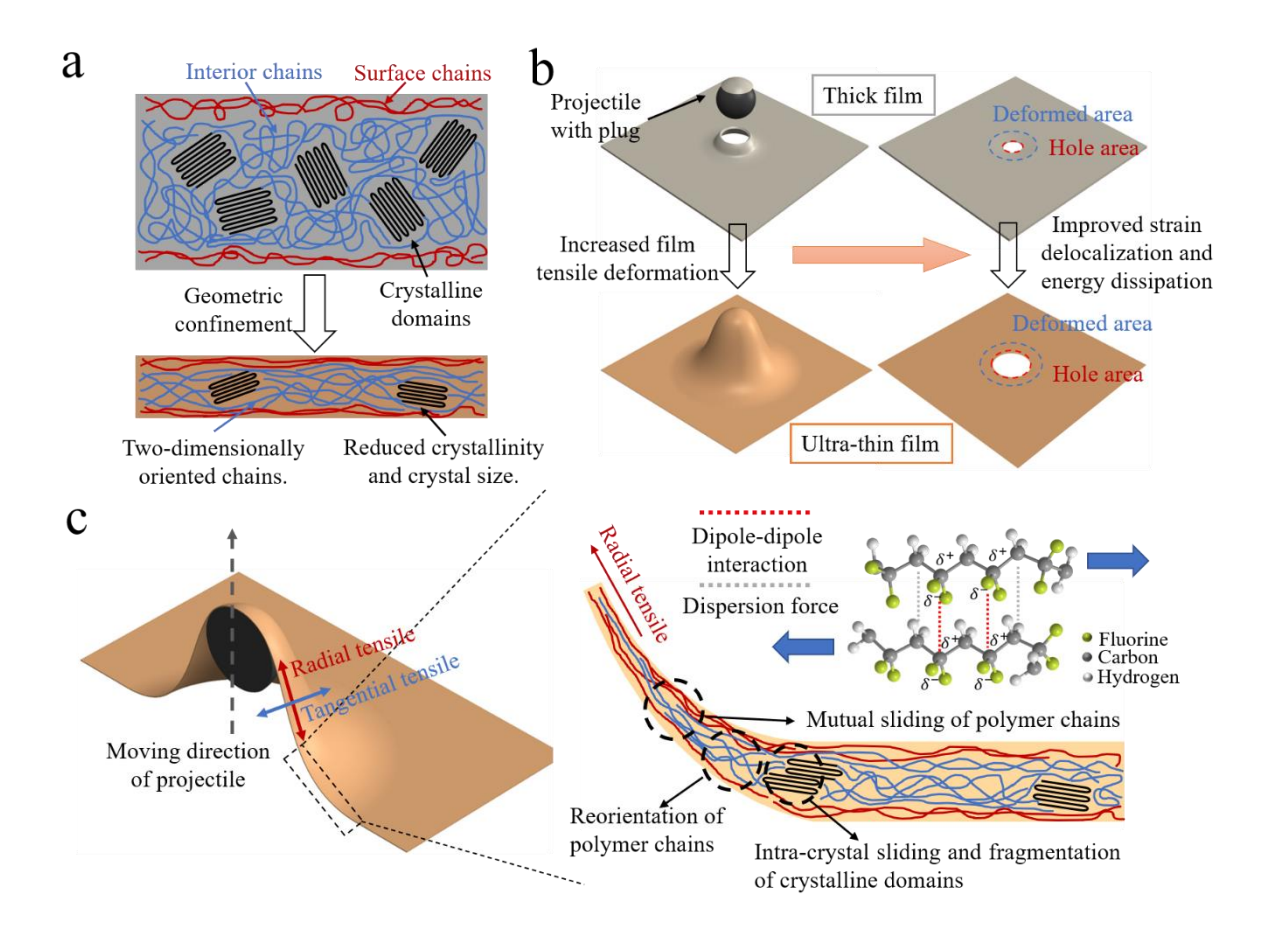


Figure 4. (a) Geometric-confinement-induced nanostructural evolution of ultra-thin P(VDF-TrFE) film, (b) Thinner polymer film exhibits higher tensile deformation, which brings in the significant improvement in strain delocalization and energy dissipation, (c) Cross-section of stretched film during projectile impact showing potential energy dissipation mechanisms, including polymer chain mutual sliding, re-orientation, flow towards the impact zone and intracrystal sliding and fragmentation of crystalline domains.

Therefore, the sub-100-nm ultra-thin non-annealed films exhibit significant ductile behavior arising from the long-range polymer chain mobility in both near-surface and interior regions. During impact, the forward moving projectile causes equibiaxial tensile stresses and viscoelastically stretches the polymer film into a conical shape, Figure 4b. This material flow into the impact region engages substantial mutual polymer chains sliding and orienting along the principal stretch directions, Figure 4c. The van der Waals (vdW) interactions are the primary bonding between nearby chains in ultra-thin P(VDF-TrFE) films. Besides the weak dispersion forces from non-polar C-H bonds, existance of relatively stronger dipole-dipole interactions from strongly polar C-F bonds increases the intermolecular attractive forces. Significant energy can be dissipated as a result of the cumulative effects of vdW interactions among polymer chains that are highly extended along the film stretching direction. At high strains, intra-crystal sliding and fragmentation of crystalline domains also start to participate in dissipating energy. Because of the low crystallinity of piezoelectrically responsive β -phase (all-trans) in ultra-thin P(VDF-TrFE) films (Fig.1(e-f)), the contribution of Coulombic interactions to energy dissipation is negligible compared to other mechanisms described above. At high strains, adiabatic heating ($T_c\sim 101$ °C) in the strike region can also deteriorate the piezoelectric effects. Synergistic interplay among these energy dissipation mechanisms leads to the observed superior E_p^* of the ultra-thin P(VDF-TrFE) films under supersonic micro-projectile impacts.

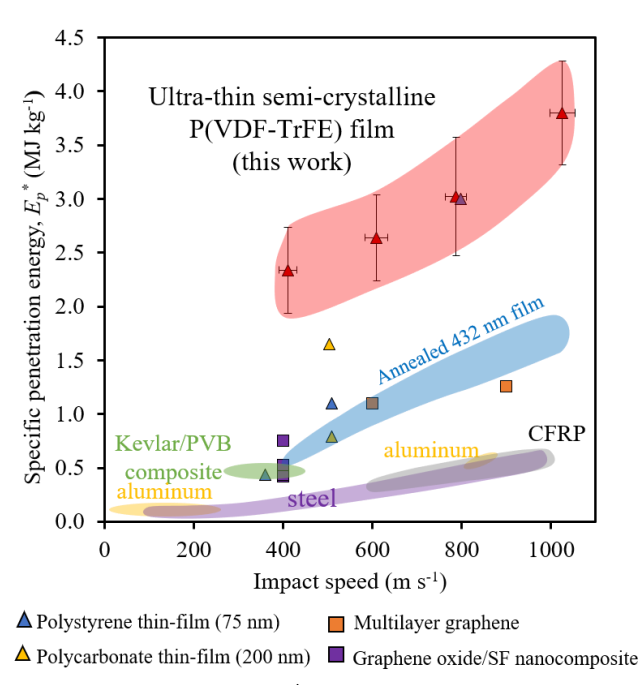


Figure 5. Specific penetration energy (E_p^*) of ultra-thin P(VDF-TrFE) films compared to annealed 432 nm-thick P(VDF-TrFE) films and other protective materials.^{8, 9, 13, 14, 36-41}

We compare the E_p^* of ultra-thin (73nm) P(VDF-TrFE) films corresponding to different projectile impact speeds to both bulk protective materials—including steel, aluminum, Kevlar/PVB composite, and carbon fiber reinforced plastics (CFRP)³⁶⁻⁴¹—from macroscopic testing, and different kinds of nanomaterials—annealed 432nm-thick P(VDF-TrFE) films (this work), polystyrene and polycarbonate thin-films, multilayer graphene, and graphene oxide nanocomposites^{8, 9, 13, 14}—from LIPIT, Figure 5. To ensure the validity of comparing our study with previous studies that utilized smaller sizes of microprojectiles in LIPIT, we additionally investigated the effects of a smaller projectile (4.08 μ m) on the E_p^* of our ultra-thin P(VDF-TrFE) films. The measured E_p^* (Figure S5) shows that the effects of projectile size are not considerable. The important experimental parameters of all these studies are summarized in Table S1 in Supporting Information. Compared to the widely used macroscopic protective materials, ultra-thin P(VDF-TrFE) films exhibit superior E_p^* across a broad range of projectile impact velocities. For instance, the E_p^* of P(VDF-TrFE) is ~5.8 times that of steel^{37, 38} and CFRP plates⁴¹ at ~1 km s⁻¹ impact, and ~4.3 times that of Kevlar/PVB composite plates³⁶ at ~400 m s⁻¹ impact. Compared to nanomaterials, the P(VDF-TrFE) polymer thin-films exhibit

significantly higher dynamic mechanical performance with distinct energy dissipation mechanisms— E_p^* of ultra-thin P(VDF-TrFE) is ~2.2 times that of the annealed 432 nm-thick P(VDF-TrFE) film (1.74 MJ kg⁻¹ at 1 km s⁻¹ impact) and ~2.7 times that of multilayer graphene (1.26 MJ kg⁻¹ at 900 m s⁻¹ impact)⁸. Although the performance of ultra-thin P(VDF-TrFE) films is comparable to PS at high impact speeds (800 m s⁻¹, with addition of direct kinetic energy transferred to plug to the reported $^9E_p^*$ to be consistent with other works 8), the P(VDF-TrFE) films exhibit outstanding performance across broad range of velocities unlike the PS—P(VDF-TrFE) exhibits much higher E_p^* (~5.4 times) at low velocity (400 m s⁻¹) impacts 9 .

In contrast to rigid protective materials, dynamic energy dissipation in polymeric materials always comes with relatively large deformations, which may result in significant behind armor blunt trauma (BABT)—a non-penetrating injury from rapid deformation of armor.⁴² This has limited the application of soft polymeric materials in ballistic protection. However, such deformable thin-films are suitable candidates for creating "ambient armors", where the armor that is made of stacked nanoscale films is placed at a standoff distance from the target which needs protection.⁴³ On the contrary to traditional armor design strategy, which utilizes ultra-strong and stiff materials to mitigate ballistic impacts, here we demonstrate that extensive viscoelastic and viscoplastic deformation of ultra-thin rubbery semi-crystalline polymer films lead to superior specific energy absorption over a broad impact velocity range from 100 m s⁻¹ to 1 km s⁻¹. For instance, to stop a projectile (diameter: 9.2µm) traveling at 1 km s⁻¹ velocity by a multi-layered stacked film (neglecting interactions between subsequent films), the required total film thickness decreases from ~4.3 µm for annealed 432 nm-thick films (10 layers) to ~1.4 µm for 73 nm-thick films (19 layers), which significantly reduces the weight of the "armor" by 67% (Figure S6; calculation method in supporting information). The layer-by-layer fabrication methods⁴⁴ for large area ultra-thin polymer films will enable scaling up of the fabrication process with multi-material components that can function in different extreme environments.

In summary, we experimentally demonstrated the superior dynamic performance of ultra-thin P(VDF-TrFE) films using an advanced LIPIT technique and correlated their E_p^* and strain delocalization performance to the material's fabrication processes and their nanostructural evolution for the first time. The highest E_p^* achieved for ultra-thin P(VDF-TrFE) film is significantly higher than that of macroscopic protective materials and previously studied nanomaterials. Geometric confinement in ultra-thin films hinders the crystallization process and facilitates the polymer chains to orient parallel to the film surface. With the contribution of those highly mobile two-dimensionally oriented polymer chains, extensive viscoelastic and viscoplastic deformation occurs during projectile penetration. The cumulative effects of relatively stronger vdW forces from the dipole-dipole interactions between polar C-F bonds in polymer chains oriented along the stretching direction further strengthens and toughens the P(VDF-TrFE) thin films. Along with local adiabatic heating within the strike region at high velocities, these deformation processes effectively dissipate the kinetic energy of the supersonic projectile. Our study opens novel design pathways for fabricating light-weight soft armor materials with superior dynamic performance by employing nanoscale semi-crystalline polymeric films with tailored micro/nanostructures.

SUPPORTING INFORMATION

Experimental details including fabrication of polymer film and post-processing treatment, dynamic mechanical performance characterization, microstructure characterization, and several complementary results are given in supporting information.

ACKNOWLEDGMENT

Support for this research was provided by the University of Wisconsin-Madison, Office of the Vice Chancellor for Research and Graduate Education with funding from the Wisconsin Alumni Research Foundation. The use of facilities and instrumentation supported by NSF through the University of Wisconsin Materials Research Science and Engineering Center

(DMR-1720415) are also acknowledged. We also thank Claire Griesbach for her assistance in performing FIB cross-sectioning of impacted samples for analysis, and Sadegh Yazdi (University of Colorado-Boulder) for useful conversations.

REFERENCES

- 1. Yadav, R.; Naebe, M.; Wang, X.; Kandasubramanian, B., Body armour materials: from steel to contemporary biomimetic systems. *Rsc Adv* **2016**, *6* (116), 115145-115174.
- 2. Lee, C.; Wei, X.; Kysar, J. W.; Hone, J., Measurement of the Elastic Properties and Intrinsic Strength of Monolayer Graphene. *Science* **2008**, *321* (5887), 385.
- 3. Peng, B.; Locascio, M.; Zapol, P.; Li, S. Y.; Mielke, S. L.; Schatz, G. C.; Espinosa, H. D., Measurements of near-ultimate strength for multiwalled carbon nanotubes and irradiation-induced crosslinking improvements. *Nat Nanotechnol* **2008**, *3* (10), 626-631.
- 4. Shrestha, R.; Li, P.; Chatterjee, B.; Zheng, T.; Wu, X.; Liu, Z.; Luo, T.; Choi, S.; Hippalgaonkar, K.; de Boer, M. P.; Shen, S., Crystalline polymer nanofibers with ultra-high strength and thermal conductivity. *Nat Commun* **2018**, *9* (1), 1664.
- 5. Cai, J.; Naraghi, M., The formation of highly ordered graphitic interphase around embedded CNTs controls the mechanics of ultra-strong carbonized nanofibers. *Acta Mater* **2019**, *162*, 46-54.
- 6. Papkov, D.; Zou, Y.; Andalib, M. N.; Goponenko, A.; Cheng, S. Z. D.; Dzenis, Y. A., Simultaneously Strong and Tough Ultrafine Continuous Nanofibers. *Acs Nano* **2013**, *7* (4), 3324-3331.
- 7. Lee, J.-H.; Veysset, D.; Singer, J. P.; Retsch, M.; Saini, G.; Pezeril, T.; Nelson, K. A.; Thomas, E. L., High strain rate deformation of layered nanocomposites. *Nat Commun* **2012**, *3*, 1164.
- 8. Lee, J.-H.; Loya, P. E.; Lou, J.; Thomas, E. L., Dynamic mechanical behavior of multilayer graphene via supersonic projectile penetration. *Science* **2014**, *346* (6213), 1092-1096.
- 9. Hyon, J.; Lawal, O.; Fried, O.; Thevamaran, R.; Yazdi, S.; Zhou, M.; Veysset, D.; Kooi, S. E.; Jiao, Y.; Hsiao, M.-S.; Streit, J.; Vaia, R. A.; Thomas, E. L., Extreme Energy Absorption in Glassy Polymer Thin Films by Supersonic Micro-projectile Impact. *Materials Today* **2018**, *21* (8), 817-824.
- 10. Cai, J.; Naraghi, M., Non-intertwined graphitic domains in nanoscale leads to super strong and tough continuous 1D nanostructures. *Carbon* **2018**, *137*, 242-251.
- 11. Yin, Z.; Hannard, F.; Barthelat, F., Impact-resistant nacre-like transparent materials. *Science* **2019**, *364* (6447), 1260-1263.
- 12. Liao, X.; Dulle, M.; de Souza e Silva, J. M.; Wehrspohn, R. B.; Agarwal, S.; Förster, S.; Hou, H.; Smith, P.; Greiner, A., High strength in combination with high toughness in robust and sustainable polymeric materials. *Science* **2019**, *366* (6471), 1376.
- 13. Xie, W.; Tadepalli, S.; Park, S. H.; Kazemi-Moridani, A.; Jiang, Q.; Singamaneni, S.; Lee, J.-H., Extreme Mechanical Behavior of Nacre-Mimetic Graphene-Oxide and Silk Nanocomposites. *Nano Lett* **2018**, *18* (2), 987-993.
- 14. Chan, E. P.; Xie, W.; Orski, S. V.; Lee, J.-H.; Soles, C. L., Entanglement Density-Dependent Energy Absorption of Polycarbonate Films via Supersonic Fracture. *ACS Macro Letters* **2019**, *8* (7), 806-811.

- 15. Xie, W.; Zhang, R.; Headrick, R. J.; Taylor, L. W.; Kooi, S.; Pasquali, M.; Müftü, S.; Lee, J.-H., Dynamic Strengthening of Carbon Nanotube Fibers under Extreme Mechanical Impulses. *Nano Lett* **2019**, *19* (6), 3519-3526.
- 16. Siviour, C. R.; Jordan, J. L., High Strain Rate Mechanics of Polymers: A Review. *Journal of Dynamic Behavior of Materials* **2016**, *2* (1), 15-32.
- 17. Jordan, J. L.; Siviour, C. R.; Foley, J. R.; Brown, E. N., Compressive properties of extruded polytetrafluoroethylene. *Polymer* **2007**, *48* (14), 4184-4195.
- 18. Brown, E. N.; Dattelbaum, D. M., The role of crystalline phase on fracture and microstructure evolution of polytetrafluoroethylene (PTFE). *Polymer* **2005**, *46* (9), 3056-3068.
- 19. Himmelberger, S.; Dacuña, J.; Rivnay, J.; Jimison, L. H.; McCarthy-Ward, T.; Heeney, M.; McCulloch, I.; Toney, M. F.; Salleo, A., Effects of Confinement on Microstructure and Charge Transport in High Performance Semicrystalline Polymer Semiconductors. *Adv Funct Mater* **2013**, *23* (16), 2091-2098.
- 20. Alcoutlabi, M.; McKenna, G. B., Effects of confinement on material behaviour at the nanometre size scale. *Journal of Physics: Condensed Matter* **2005**, *17* (15), R461-R524.
- 21. Lee, J.-H.; Chung, J. Y.; Stafford, C. M., Effect of Confinement on Stiffness and Fracture of Thin Amorphous Polymer Films. *ACS Macro Letters* **2012**, *I* (1), 122-126.
- 22. Ico, G.; Showalter, A.; Bosze, W.; Gott, S. C.; Kim, B. S.; Rao, M. P.; Myung, N. V.; Nam, J., Size-dependent piezoelectric and mechanical properties of electrospun P(VDF-TrFE) nanofibers for enhanced energy harvesting. *J Mater Chem A* **2016**, *4* (6), 2293-2304.
- 23. Baniasadi, M.; Huang, J.; Xu, Z.; Moreno, S.; Yang, X.; Chang, J.; Quevedo-Lopez, M. A.; Naraghi, M.; Minary-Jolandan, M., High-Performance Coils and Yarns of Polymeric Piezoelectric Nanofibers. *Acs Appl Mater Inter* **2015**, *7* (9), 5358-5366.
- 24. Xu, Z.; Baniasadi, M.; Moreno, S.; Cai, J.; Naraghi, M.; Minary-Jolandan, M., Evolution of electromechanical and morphological properties of piezoelectric thin films with thermomechanical processing. *Polymer* **2016**, *106*, 62-71.
- 25. Frank, C. W.; Rao, V.; Despotopoulou, M. M.; Pease, R. F. W.; Hinsberg, W. D.; Miller, R. D.; Rabolt, J. F., Structure in Thin and Ultrathin Spin-Cast Polymer Films. *Science* **1996**, *273* (5277), 912.
- 26. Zhang, Q. M.; Xu, H.; Fang, F.; Cheng, Z. Y.; Xia, F.; You, H., Critical thickness of crystallization and discontinuous change in ferroelectric behavior with thickness in ferroelectric polymer thin films. *J Appl Phys* **2001**, *89* (5), 2613-2616.
- 27. Xia, F.; Razavi, B.; Xu, H.; Cheng, Z. Y.; Zhang, Q. M., Dependence of threshold thickness of crystallization and film morphology on film processing conditions in poly(vinylidene fluoride-trifluoroethylene) copolymer thin films. *J Appl Phys* **2002**, *92* (6), 3111-3115.
- 28. Guo, D.; Setter, N., Impact of Confinement-Induced Cooperative Molecular Orientation Change on the Ferroelectric Size Effect in Ultrathin P(VDF-TrFE) Films. *Macromolecules* **2013**, *46* (5), 1883-1889.
- 29. Jones, R. L.; Kumar, S. K.; Ho, D. L.; Briber, R. M.; Russell, T. P., Chain conformation in ultrathin polymer films. *Nature* **1999**, *400* (6740), 146-149.
- 30. Teyssedre, G.; Bernes, A.; Lacabanne, C., DSC and TSC study of a VDF/TrFE copolymer. *Thermochimica Acta* **1993**, *226*, 65-75.
- 31. Siviour, C. R.; Walley, S. M.; Proud, W. G.; Field, J. E., The high strain rate compressive behaviour of polycarbonate and polyvinylidene difluoride. *Polymer* **2005**, *46* (26), 12546-12555.
- 32. Walley, S. M.; Field, J. E., Strain rate sensitivity of polymers in compression from low to high rates. *DYMAT J* **1994**, *1*, 211-227.
- 33. Richeton, J.; Ahzi, S.; Vecchio, K. S.; Jiang, F. C.; Adharapurapu, R. R., Influence of temperature and strain rate on the mechanical behavior of three amorphous polymers:

- Characterization and modeling of the compressive yield stress. *International Journal of Solids and Structures* **2006**, *43* (7), 2318-2335.
- 34. Pu, Y.; Rafailovich, M. H.; Sokolov, J.; Gersappe, D.; Peterson, T.; Wu, W. L.; Schwarz, S. A., Mobility of Polymer Chains Confined at a Free Surface. *Phys Rev Lett* **2001**, 87 (20), 206101.
- 35. Si, L.; Massa, M. V.; Dalnoki-Veress, K.; Brown, H. R.; Jones, R. A., Chain entanglement in thin freestanding polymer films. *Phys Rev Lett* **2005**, *94* (12), 127801.
- 36. Lee, B. L.; Walsh, T. F.; Won, S. T.; Patts, H. M.; Song, J. W.; Mayer, A. H., Penetration Failure Mechanisms of Armor-Grade Fiber Composites under Impact. *Journal of Composite Materials* **2001**, *35* (18), 1605-1633.
- 37. Dean, J.; Dunleavy, C. S.; Brown, P. M.; Clyne, T. W., Energy absorption during projectile perforation of thin steel plates and the kinetic energy of ejected fragments. *International Journal of Impact Engineering* **2009**, *36* (10), 1250-1258.
- 38. Yungwirth, C. J.; O'Connor, J.; Zakraysek, A.; Deshpande, V. S.; Wadley, H. N. G., Explorations of Hybrid Sandwich Panel Concepts for Projectile Impact Mitigation. *Journal of the American Ceramic Society* **2011**, *94* (s1), s62-s75.
- 39. Golsdmith, W.; Finnegan, S. A., Penetration and perforation processes in metal targets at and above ballistic velocities. *International Journal of Mechanical Sciences* **1971**, *13* (10), 843-866.
- 40. Gupta, N. K.; Iqbal, M. A.; Sekhon, G. S., Experimental and numerical studies on the behavior of thin aluminum plates subjected to impact by blunt- and hemispherical-nosed projectiles. *International Journal of Impact Engineering* **2006**, *32* (12), 1921-1944.
- 41. Fujii, K.; Aoki, M.; Kiuchi, N.; Yasuda, E.; Tanabe, Y., Impact perforation behavior of CFRPs using high-velocity steel sphere. *International Journal of Impact Engineering* **2002**, 27 (5), 497-508.
- 42. Cannon, L., Behind armour blunt trauma--an emerging problem. *Journal of the Royal Army Medical Corps* **2001**, *147* (1), 87-96.
- 43. Liu, P.; Strano, M. S., Toward Ambient Armor: Can New Materials Change Longstanding Concepts of Projectile Protection? *Adv Funct Mater* **2016**, *26* (6), 943-954.
- 44. Richardson, J. J.; Björnmalm, M.; Caruso, F., Technology-driven layer-by-layer assembly of nanofilms. *Science* **2015**, *348* (6233), aaa2491.

Supporting Information

Superior Energy Dissipation by Ultra-thin Semicrystalline Polymer Films Under Supersonic Micro-Projectile Impacts

Jizhe Cai and Ramathasan Thevamaran*

Department of Engineering Physics, University of Wisconsin-Madison, Madison, WI 53706, United States

*corresponding author: thevamaran@wisc.edu

Fabrication of polymer film and post-processing treatment:

The free-standing P(VDF-TrFE) thin-films were prepared by spinning coating. First, different amounts of P(VDF-TrFE) (70/30) copolymer (Piezotech® FC30, M_w: 450,000 g mol⁻¹) were dissolved in the dimethylformamide (DMF) solvent (99.8%, Sigma-Aldrich) via magnetic stirring at 70°C for about 8 hours. Then, acetone (Electronic grade, Fisher Chemical) was added to the polymer/DMF solution and magnetic stirred for about 3 hours until a visually homogenous solution is obtained. The polymer solution with different P(VDF-TrFE) concentrations (3-8 wt.%) were prepared. A 3-inch silicon wafer treated with polyectrolyte polydiallyldimethylammonium chloride (PDAC) (Sigma-Aldrich, M_w: 1×10⁵ - 2×10⁵ g mol⁻¹), was used as the substrate to fabricate polymer films in a spin-coater (Laurell WS-650-23B). Polymer solution (1-2 mL) was dropped on the rotating silicon wafer (300 rpm), then spun for 60 s at 3000 - 5000 rpm. Polymer films with different thicknesses (73, 165, and 432 nm) were fabricated using different concentrations of polymer solution. The film thickness was obtained by measuring the height between the substrate and the film top surface across a cut step on the film using an atomic force microscope (AFM Bruker BioScope Catalyst). The silicon wafer with polymer films were slowly immersed into deionized water to detach the polymer film from

the wafer and float on the water surface, which is then collected on a metallic hoop. To promote the formation of crystalline structures, the as-fabricated 79 nm and 432 nm thick film is annealed at 125 °C for 1 hour. The annealing temperature is chosen to be 125 °C, being above the Curie temperature ($T_c = 101$ °C), and below the melting temperature ($T_m = 150$ °C) of P(VDF-TrFE), which promotes the formation of crystalline structure within polymer films.² The free-standing polymer films with different thicknesses and post-processing treatments were deposited on TEM grids with epoxy glue for subsequent LIPIT.

Dynamic mechanical performance characterization:

Monodisperse silica microspheres with 9.2 μm diameter (Cospheric) were dispersed in ethanol solvent via vortex mixing. The solution was drop casted and air dried on the launch pad—a microscope glass slide coated with 50 nm-thick gold followed by about 30 μm PDMS. An Nd-YAG ablation laser (Spectra-Physics Quanta-Ray INDI-40-10-HG) was used to launch projectile. The gold layer in the launch pad was ablated by a single laser pulse (6-9 ns pulse width, 1064 nm) to rapidly expand the PDMS layer which selectively launches an individual micro-projectile towards the sample placed at ~500 μm from the launch pad. The ablation laser energy is calibrated to launch the projectile at desired control speeds from 100 m s⁻¹ to 1 km s⁻¹. A super-continuum white laser (NKT Photonics SuperK EXR-20) with pulse intervals of 103-154 ns gated by an acousto-optic modulator (ISOMET 1250C-848) is used to provide the illumination pulses for multi-exposure imaging of the projectile in flight on a monochromatic camera (Allied Vision Mako G-234B). About 10 impact experiments were performed for each film thickness and impact velocity.

Microstructure characterization:

The post-impact deformation micro/nanostructures of polymer films were imaged by Zeiss LEO 1550 VP scanning electron microscope (SEM). The X-ray diffraction spectrum (CuKα, wavelength of 0.154 nm) of the P(VDF-TrFE) films with different thicknesses and post-treatments were obtained using Bruker D8 Discover X-ray diffractometer. The crystallinity was

calculated based on the relative area under the deconvoluted amorphous and crystalline peaks and the crystal size was calculated using Scherrer equation (K = 0.9).

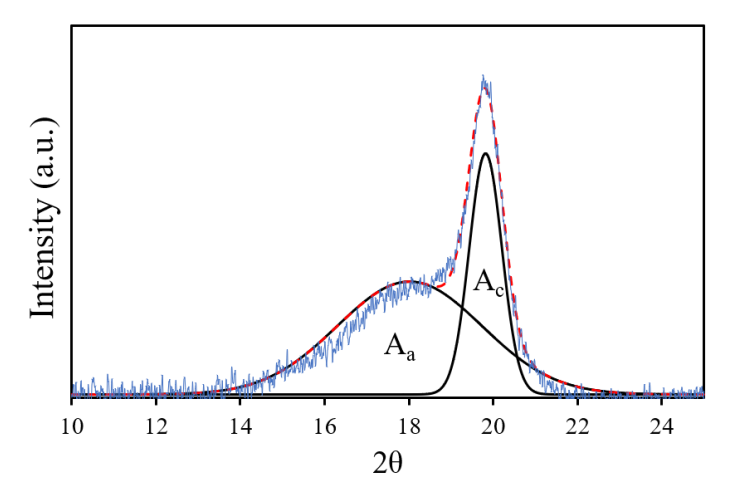


Figure S1. Representative analysis of the XRD spectra of a non-annealed 432 nm-thick film.

The crystallinity of polymer film is calculated by dividing the area under the peak from crystalline phase (A_c) by the total area under the whole curve $(A_a + A_c)$.

Crystallinity (%) =
$$\frac{A_c}{A_a + A_c}$$
 (1)

The crystal size within each polymer film is calculated using Scherrer equation:

$$t = \frac{0.9\lambda}{B\cos(\theta)} \tag{2}$$

where t is the thickness of the lamellar crystals (crystal size), λ is the X-ray wavelength, B is the full width at half maximum for the diffraction peak and θ is the half of the diffraction angle.

Post-impact zone SEM images:

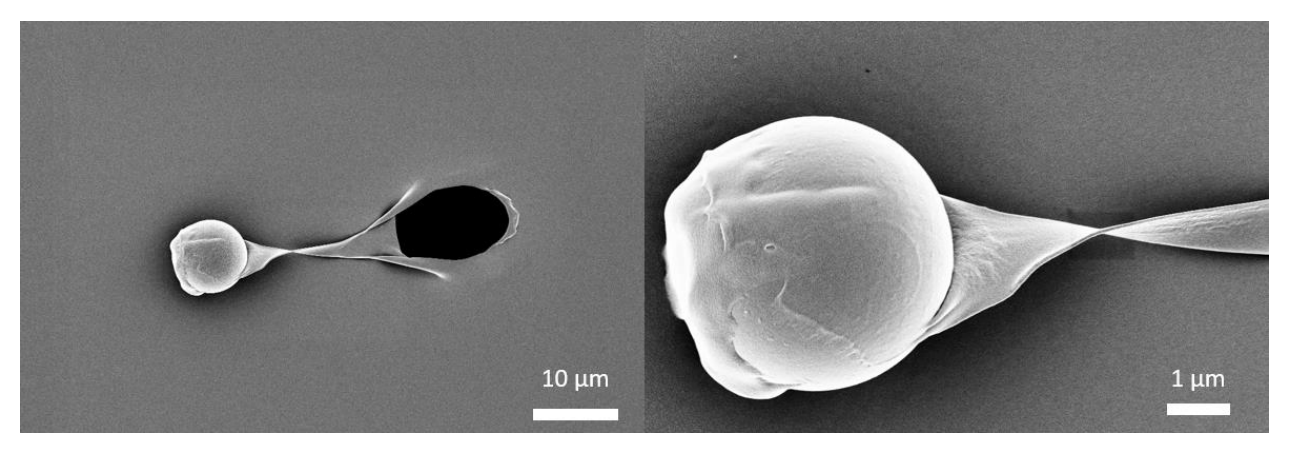


Figure S2. A projectile attached to the film showing the substantial stretching of the film and the polymer melt from impact around the projectile (Thickness = 165 nm)

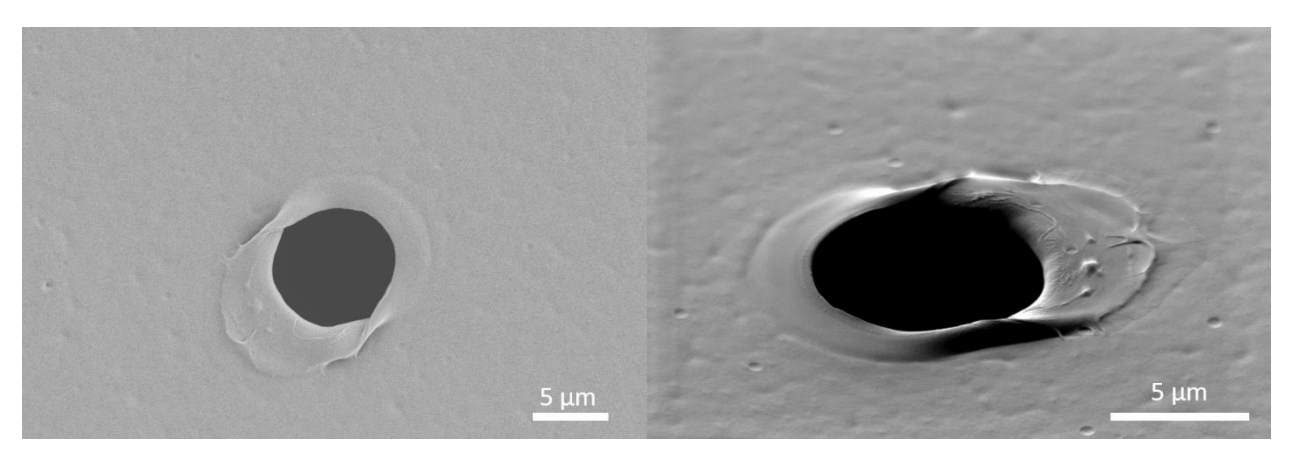


Figure S3. Failure zone images of 432-nm-thick film with 600 m s⁻¹ impact.

Strain rate calculation:

During the film perforation process, the strain rate is approximated by,

$$\frac{\Delta \varepsilon}{\Delta t} \cong \frac{\varepsilon_{max}}{t_p} \cong \frac{t_p}{2} \left(\frac{v_i}{R_c}\right)^2 \tag{3}$$

where $\varepsilon_{max} \cong \left(\frac{v_i t_p}{R_c}\right)^2/2$, based on the 1-D approximation of the maximum tensile strain for isotropic membrane with biaxial deformation. R_c is the deformation cone radius, which is obtained from the radius of the circle enclosing deformed area. t_p is the perforation time of the projectile, which is approximately equal to the ratio between cone radius and cone velocity. The cone velocity is calculated by $v_c \cong 1.23c_{||}(v_i/(\sqrt{2}c_{||}))^{2/3}$, where $c_{||}$ is the in-plane sound speed in the materials, which is directly related to the plane-strain elastic modulus (0.55 GPa)

² and mass density of the polymer (1795 kg m⁻³). Therefore, the calculated strain rate for 73 nm-thick film with 400 and 1000 m s⁻¹ impacts are 1.9×10^7 and 9.6×10^7 S⁻¹, respectively.

Air-drag Velocity Corrections:

To obtain accurate ΔKE , we consider two major sources of energy dissipation: projectile air-drag during flight and air drag due to target film deformation by the forward-moving projectile before perforation.

1) Projectile air-drag in flight:

During the flight of projectile, air-drag acts in the opposite direction to the relative motion of the projectile with respect to surrounding air. Air-drag dependents on the in-flight projectile velocity. To accurately measure the speeds of the projectile right before and after perforation of the target, we first measure the air drag coefficient as a function of projectile velocity from our experiments. The method is similar to that of described in the supporting information of Hyon J, et al.⁴

The equation of projectile motion is described by,

$$m\frac{dv}{dt} = -\frac{1}{2}C_D\rho_{air}Av^2 \tag{4}$$

where m is the weight of projectile, v is velocity, C_D is the drag coefficient, ρ_{air} is the density of air (1.20 kg/m³), A is the cross-sectional area of the projectile. The C_D of projectile is dependent on geometry of projectile and the Reynolds number ($R_e \sim 360 - 600$).

The projectile trajectory equation is given by,

$$x(t) = \frac{1}{B} \left[\ln \left(t - t_0 + \frac{1}{Bv_0} \right) - \ln \left(\frac{1}{Bv_0} \right) \right] + x_0$$
 (5)

where $B = \frac{C_D \rho_{air} A}{2m}$, and v_0 is the velocity at time t_0 . To calculate the drag coefficient, the trajectories of the projectiles were determined from the multi-exposure optical images of the projectiles launched at 1 km s⁻¹, 800 m s⁻¹, and 600 m s⁻¹. Using the position and time of the first recorded projectile as the reference time (t_0) and position (x_0) , the trajectories were fitted to find the drag coefficients, see Figure S4 for the 1 km s⁻¹ projectile. The obtained drag

coefficient of the projectile at 1 km s⁻¹ is ~0.42. For projectiles traveling at 800 m s⁻¹ and 600 m s⁻¹, the drag coefficients are ~0.46 and 0.48, respectively. For the low speed projectile impact ($< 400 \text{ m s}^{-1}$), the effect of air-drag-induced projectile deceleration is negligible compared to the perforation-induced decrease in speed. Therefore, the speed correction is only performed for the high-speed projectile impacts ($\ge 600 \text{ m s}^{-1}$). To correct the impact and residual speeds of projectile for the air drag, first the impact and residual speeds of projectile were calculated by dividing the distances between adjacent snapshots of the projectile right before and after perforation by the known time interval (102.6 ns). Then, the corrected impact speed is calculated by subtracting the speed decrease due to air drag (Equation 4) during the travel distance between the last projectile location and the target ($\sim 150 \text{ }\mu\text{m}$). The corrected residual speed of the projectile is obtained by similar approach by adding the air-drag-induced speed decrease to the residual speed directly measured from the first two projectile snapshots post-penetration.

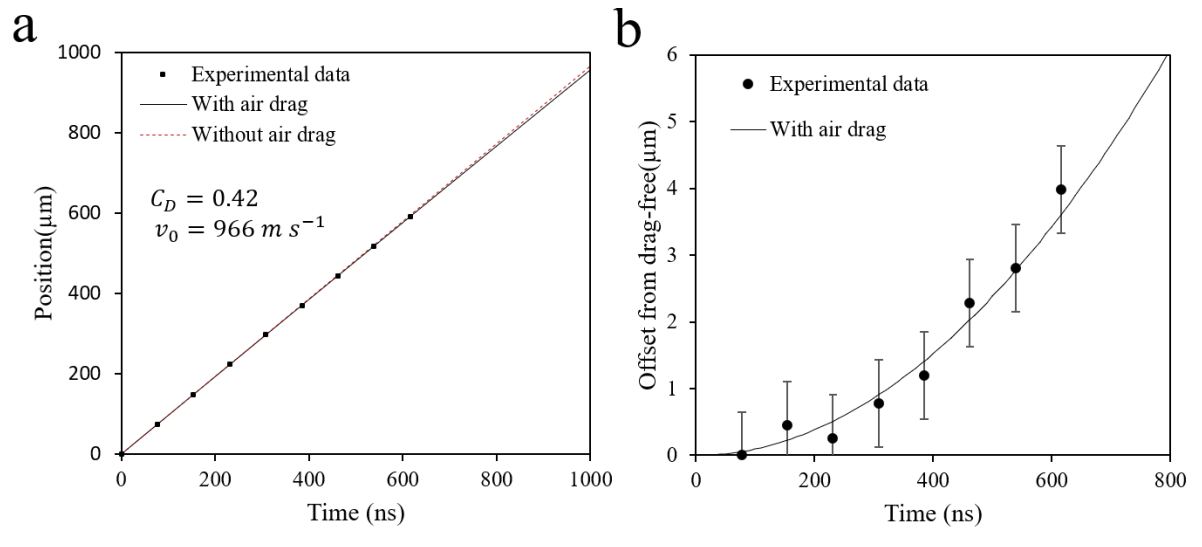


Figure S4. Experimentally obtained projectile trajectory (solid square) and fitted trajectory (black solid line). The trajectory of projectile without air drag is represented as the red dashed line. (b) The projectile trajectory deviation from the drag-free condition.

2) Film air-drag:

The energy dissipation due to drag force from the deforming film during the projectile penetration is calculated by ⁴:

$$E_{drag} = \int_{0}^{D} \frac{1}{2} \rho_{air} C_{D} \pi v_{cone}^{2} x^{2} dx = \frac{1}{2} \rho_{air} C_{D} \pi v_{cone}^{2} \frac{D^{3}}{3}$$

where the distance traveled by the projectile, $D \sim t_p v_i \approx 8 \, \mu m$, for 73 nm thick film at 1km/s impact. ρ_{air} is air density (1.20 kg/m³). $C_D = 1.3$ for film. v_{cone} is the base speed of the expanding thin-film cone, which is ~800 m s⁻¹. Therefore, the calculated E_{drag} is about 0.27 nJ, which is a conservative estimate of the film air drag. This is significantly less than the measured energy dissipations, therefore neglected.

Effect of projectile size on results:

To ensure the validity of comparing various literature on LIPIT performed using different projectile sizes, we also performed experiments on the ultra-thin (79 nm) film with a smaller projectile (diameter = $4.08 \mu m$). The air-drag coefficient C_D for the $4.08 \mu m$ projectile is obtained following the process described in the previous section, which are 0.51, 0.50, 0.46 and 0.44 at 400, 600, 800 and 1000 m s^{-1} , respectively. Following the air drag correction for the impact and residual speeds, the specific penetration energy of the ultra-thin films (thickness = 79 nm) is obtained. The comparison between results from $9.2 \mu m$ and $4.08 \mu m$ projectile impacts is shown in Figure S5. The results demonstrate that changing projectile size from $9.2 \mu m$ to $4.08 \mu m$ does not cause significant difference in the specific penetration energy.

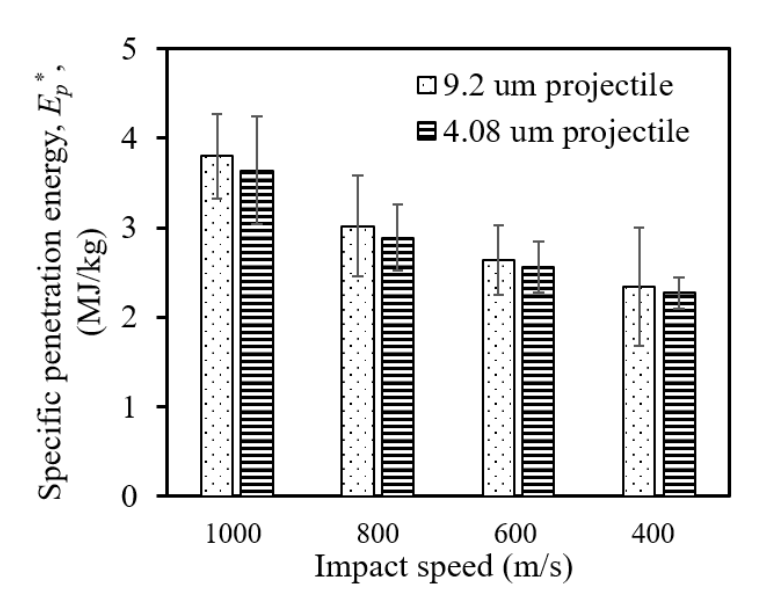


Figure S5. Comparison of specific penetration energy of thin P(VDF-TrFE) films impacted at different projectile impact speeds and with different projectile sizes.

Calculation of end-to-end distance:

The end-to-end distance of polymer chains within amorphous phase in the polymer film is calculated by using following equation,

$$R_0 = \langle R^2 \rangle^{1/2} = N^{1/2} C_{\omega}^{1/2} l$$

where R_0 is the RMS end-to-end distance of the polymer chains with N bonds. l is 1.54 Å for C-C bonds. Characteristic ratio, C_{∞} , of P(VDF-TrFE) is assumed to be similar to PVDF, which is about 6.9 5 . Then, the end-to-end distance is calculated to be 46 nm.

Protective performances prediction of stacked films:

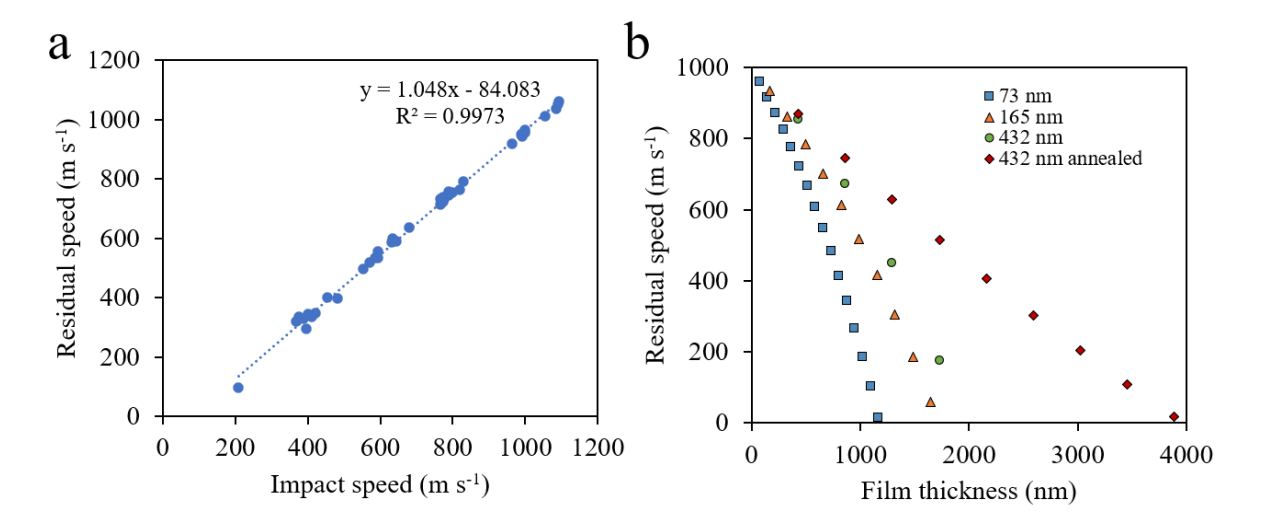


Figure S6. (a) Linear fitting of residual speed versus impact speed of 73 nm-thick film. (b) Calculated projectile residual velocities after perforating stacked films with different thicknesses, based on 73 nm, 165 nm and 432 nm-thick films, upon 1 km s⁻¹ impact.

Based on the experimentally measured residual speeds of projectiles after perforating a single layer film at various impact speeds (from about 200 m⁻¹ to 1 km s⁻¹, Figure 2c), the linear fits of residual speeds versus impact speeds of different thin films are obtained, an example of 73 nm film is shown in Figure S6a. By assuming the initial impact speed of a 9.2 µm projectile to be 1 km s⁻¹, the residual speed of projectile after perforating P(VDF-TrFE) film can be obtained from the experimental fit. Then, this residual speed is used as the impact speed for the second layer of film to calculate the residual speed after perforating that second layer. By iteratively using this approach (neglecting any interaction between subsequent films), the relationship between residual speed of projectile and the thickness of the number of films is obtained (shown in Figure S6b). The total number of layers that is required to stop the projectile is obtained when the residual speed of the projectile becomes zero.

Table S1. Comparison of experimental parameters of LIPIT and macroscopic ballistic tests on various materials. ^{4, 6-14}

Target materials	Projectile parameters	Impact speeds	Air drag correction methods	Reference
LIPIT				

P(VDF-TrFE)	silica sphere	200 – 1000	With air drag	This work		
t = 73 - 432 nm	d = 9.2 μm	m/s	calibration: $C_d = 0.48-0.44$			
Polystyrene (PS) film	silica sphere	350 – 800	With air drag	[4]		
		m/s	calibration:	L · J		
t = 75-290 nm	$d = 3.7 \mu m$		$C_d = 0.5 - 0.45$			
Polycarbonate (PC) film	silica sphere	~ 500 m/s	Conducted in	[6]		
			vacuum to minimize			
t = 140-271 nm	d = 7.6 μm		air drag			
Multilayer graphene	silica sphere	600, 900 m/s	With air drag calibration:	[7]		
t = 10-100 nm	$d = 3.7 \mu m$		$C_d = \sim 0.5$			
Graphene/silk fibroin	silica sphere	400 m/s	none	[8]		
nanocomposite						
t = 80-150 nm	$d = 7.6 \mu m$					
Macroscopic ballistic testing						
Kevlar KM2/phenolic-	Tungsten carbide	298-422 m/s	N/A	[9]		
polyvinylbutyral 50/50	sphere					
resin composite						
t = 4.7 mm	d = 12.7 mm					
304 stainless steel	Steel sphere	176-592 m/s	N/A	[10]		
t = 0.4 mm	d = 8 mm					
304 stainless steel	Steel sphere	480-997 m/s	N/A	[11]		
t = 3 mm	d = 12.5 mm					
Aluminum	Steel sphere	151-284 m/s	N/A	[12]		
	d = 12.7 mm and	and 201-853				
t = 1.27 mm	6.35 mm	m/s				
Aluminum	Steel hemispherical	92-115 m/s	N/A	[13]		
	projectile					
t = 1 mm	d = 19 mm	700 100	27/1	54.43		
Carbon Fiber Reinforced	Steel sphere	500 -1230	N/A	[14]		
Plastics (CFRPs)		m/s				
t = 2 and 6 mm	d = 4 mm					

References

- 1. Baxamusa, S. H.; Stadermann, M.; Aracne-Ruddle, C.; Nelson, A. J.; Chea, M.; Li, S.; Youngblood, K.; Suratwala, T. I., Enhanced Delamination of Ultrathin Free-Standing Polymer Films via Self-Limiting Surface Modification. *Langmuir* **2014**, *30* (18), 5126-5132.
- 2. Xu, Z.; Baniasadi, M.; Moreno, S.; Cai, J.; Naraghi, M.; Minary-Jolandan, M., Evolution of electromechanical and morphological properties of piezoelectric thin films with thermomechanical processing. *Polymer* **2016**, *106*, 62-71.
- 3. Cai, J.; Chawla, S.; Naraghi, M., Microstructural evolution and mechanics of hotdrawn CNT-reinforced polymeric nanofibers. *Carbon* **2016**, *109*, 813-822.
- 4. Hyon, J.; Lawal, O.; Fried, O.; Thevamaran, R.; Yazdi, S.; Zhou, M.; Veysset, D.; Kooi, S. E.; Jiao, Y.; Hsiao, M.-S.; Streit, J.; Vaia, R. A.; Thomas, E. L., Extreme Energy Absorption in Glassy Polymer Thin Films by Supersonic Micro-projectile Impact. *Materials Today* **2018**, *21* (8), 817-824.
- 5. Bicerano, J., *Prediction of polymer properties*. Marcel Dekker: New York, 2002.

- 6. Chan, E. P.; Xie, W.; Orski, S. V.; Lee, J.-H.; Soles, C. L., Entanglement Density-Dependent Energy Absorption of Polycarbonate Films via Supersonic Fracture. *ACS Macro Letters* **2019**, *8* (7), 806-811.
- 7. Lee, J.-H.; Loya, P. E.; Lou, J.; Thomas, E. L., Dynamic mechanical behavior of multilayer graphene via supersonic projectile penetration. *Science* **2014**, *346* (6213), 1092-1096.
- 8. Xie, W.; Tadepalli, S.; Park, S. H.; Kazemi-Moridani, A.; Jiang, Q.; Singamaneni, S.; Lee, J.-H., Extreme Mechanical Behavior of Nacre-Mimetic Graphene-Oxide and Silk Nanocomposites. *Nano Lett* **2018**, *18* (2), 987-993.
- 9. Lee, B. L.; Walsh, T. F.; Won, S. T.; Patts, H. M.; Song, J. W.; Mayer, A. H., Penetration Failure Mechanisms of Armor-Grade Fiber Composites under Impact. *Journal of Composite Materials* **2001**, *35* (18), 1605-1633.
- 10. Dean, J.; Dunleavy, C. S.; Brown, P. M.; Clyne, T. W., Energy absorption during projectile perforation of thin steel plates and the kinetic energy of ejected fragments. *International Journal of Impact Engineering* **2009**, *36* (10), 1250-1258.
- 11. Yungwirth, C. J.; O'Connor, J.; Zakraysek, A.; Deshpande, V. S.; Wadley, H. N. G., Explorations of Hybrid Sandwich Panel Concepts for Projectile Impact Mitigation. *Journal of the American Ceramic Society* **2011**, *94* (s1), s62-s75.
- 12. Golsdmith, W.; Finnegan, S. A., Penetration and perforation processes in metal targets at and above ballistic velocities. *International Journal of Mechanical Sciences* **1971**, *13* (10), 843-866.
- 13. Gupta, N. K.; Iqbal, M. A.; Sekhon, G. S., Experimental and numerical studies on the behavior of thin aluminum plates subjected to impact by blunt- and hemispherical-nosed projectiles. *International Journal of Impact Engineering* **2006**, *32* (12), 1921-1944.
- 14. Fujii, K.; Aoki, M.; Kiuchi, N.; Yasuda, E.; Tanabe, Y., Impact perforation behavior of CFRPs using high-velocity steel sphere. *International Journal of Impact Engineering* **2002**, 27 (5), 497-508.